Hydrothermally stable Pd/SiO2@Zr Core@Shell catalysts for diesel oxidation applications

Chih-Han Liu, Junjie Chen, Todd Toops, Jae-Soon Choi, Cyril Thomas, Michael Lance, Eleni Kyriakidou

Hydrothermally Stable Pd/SiO_2@Zr Core@Shell Catalysts for Diesel Oxidation Applications

Chih-Han Liu[a,+], Junjie Chen[a,+], Todd J. Toops[b], Jae-Soon Choi[b,1], Cyril Thomas[c], Michael J. Lance[b], and Eleni A. Kyriakidou[a,*]

[a] *Department of Chemical and Biological Engineering, University at Buffalo, The State University of New York, Buffalo, NY 14260, USA*

[b] *Oak Ridge National Laboratory, Oak Ridge, TN 37831, USA*

[c] *Sorbonne Université, CNRS, Laboratoire de Réactivité de Surface (LRS), 4 Place Jussieu, F-75252 Paris, France*

[+]These authors contributed equally to this work

[1]Present address: Catalyst Development Center, Basic Materials and Chemicals R&D, LG Chem, Daejeon, Korea.

[*]Corresponding author at: elenikyr@buffalo.edu (E.A. Kyriakidou)

Abstract

Hydrothermally stable diesel oxidation catalysts (DOCs) with improved low-temperature activity are desired for the abatement of emissions from diesel vehicles. Herein, novel palladium(Pd)/SiO_2(core)@Zr(shell) structured DOCs were developed. SiO_2 was completely covered by an 8.4 nm thickness Zr-based shell using a hard template method. The SiO_2@Zr support was decorated by Pd and evaluated under a simulated diesel exhaust stream. Degreened 1 wt.% Pd/SiO_2@Zr achieved 90% CO and total hydrocarbon conversion at 178 and 372 °C, respectively (feed: 6% CO_2, 12% O_2, 6% H_2O, 400 ppm H_2, 2000 ppm CO, 100 ppm NO, 1667 ppm C_2H_4, 1000 ppm C_3H_6, 333 ppm C_3H_8; HCs in C_1 basis and GHSV = 113,000 h^{-1}). After hydrothermal aging, only a minor deactivation was observed, while the surface area of 1 wt.% Pd/SiO_2@Zr was as high as 104 m^2/g. The hydrothermal stability of 1 wt.% Pd/SiO_2@Zr was attributed to the poor crystallinity of SiO_2@Zr, possibly due to the formation of Si-O-Zr bonds. This work highlights the promising potential of utilizing durable Pd/SiO_2@Zr catalysts for diesel oxidation applications.

Keywords: diesel oxidation catalyst; heterogeneous catalysis; hydrothermal stability; oxidation; core@shell

1. Introduction

Future aftertreatment systems will need to perform efficiently at increasingly low exhaust temperatures [1-3]: this so-called "150 °C challenge [4]" (i.e., achieve over 90% conversion below 150 °C) arises from continued improvements in engines efficiency and increasingly strict emission standards. An aftertreatment system normally consists of a diesel oxidation catalyst (DOC) for the oxidation of CO and hydrocarbons (HCs), a diesel particulate filter for the oxidation of particulate matter, and a selective catalytic reduction (SCR) catalyst for the reduction of NO_x to N_2 [5-7]. A DOC is required to survive hydrothermal aging at 800 °C/50 h under a feed of 10% O_2, 5% H_2O, 5% CO_2 that represents the in-use durability of a catalyst based on the low temperature aftertreatment protocol defined by U.S. DRIVE [8-10]. Under this severe aging condition, active metals tend to sinter resulting in loss of their catalytic activity [11-13]. Enhancing the metal-support interaction has shown to prevent active metal sintering [14-16]. For example, Kim et al. pretreated Pt-TiO_2 under a H_2 atmosphere at various reduction temperatures, and the results showed that pretreatment at 600 °C led to a higher CO conversion (100%) compared to a lower CO conversion (10%) achieved at room temperature when the catalyst was pretreated at 300 °C [16]. This behavior was attributed to the strong metal (Pt)-support (TiO_2) interaction (SMSI) occurring after pretreatment at temperatures > 500 °C, evidenced by the formation of smaller Pt particles (2.2-4.4 nm) compared to larger Pt particles (4.7-5.9 nm) formed after pretreatments at temperatures < 500 °C. ZrO_2 was reported to have SMSI with platinum group metals (PGMs), commonly used in DOCs [17-19]. SMSI between PGMs and ZrO_2 lead to high PGM dispersion and thus an improved DOC activity. Specifically, the $T_{50,90}$'s (temperature of 50 and 90% conversion) over 1 wt.% Pd/ZrO_2 were as low as 160, 180 °C for CO and 180, 195 °C for propylene (C_3H_6), respectively [20]. However, Pd/ZrO_2 suffers from a severe surface area loss from 93 m^2/g

(500 °C/2 h, 10% H_2/Ar) to 24 m^2/g (hydrothermal aging, 800 °C/16 h, 10% O_2, 5% H_2O/Ar) due to the growth of the mean ZrO_2 crystallite size [20]. The ZrO_2 surface area loss can be prevented by incorporating oxides with higher crystallization temperature than ZrO_2 (~150 °C [21]), e.g. Al_2O_3 (850-900 °C [22]) or SiO_2 (1000-1400 °C [23, 24]) [25]. Specifically, Al_2O_3-ZrO_2 and ZrO_2-SiO_2 have a crystallization temperature of 700 and 800 °C, respectively [21, 26]. Thus, ZrO_2-SiO_2 mixed oxide supports were utilized considering the exhaust temperature (500-700 °C) of diesel engines at 100% load [20, 27, 28]. Specifically, Kim et al. showed that hydrothermally aged (HTA) (800 °C/16 h) Pd/ZrO_2-SiO_2 had a T_{50} and T_{90} for CO at 280 and 320 °C and for C_3H_6 at 307 and 332 °C, respectively [20]. Furthermore, incorporation of SiO_2, as an acidic support, is known to improve the sulfur tolerance of the catalyst compared to bare ZrO_2 [20]. However, uncontrolled synthesis of ZrO_2-SiO_2 by a sol-gel method resulted in segregation of SiO_2 and ZrO_2, leading to formation of large Pd particles on exposed SiO_2 surfaces due to weak Pd-SiO_2 interaction. Specifically, the Pd particle size over Pd/ZrO_2, Pd/ZrO_2-SiO_2, Pd/SiO_2 increased from 1.1 nm to 1.9 nm to 4.1 nm, respectively [20]. Therefore, a complete coverage of SiO_2 by a Zr-based shell is required to prevent Pd deposition on SiO_2 and thus enhance the diesel oxidation performance of Pd/ZrO_2-SiO_2 catalysts.

Herein, SiO_2(core)@Zr(shell) supports were synthesized, where SiO_2 spheres were covered by a Zr-based shell. This was achieved by a hard template method as reported previously (Fig. 1) [3], where the SiO_2 core acted as a scaffold for the growth of the Zr-based shell layer. Pd was deposited on the SiO_2@Zr support by wet-impregnation resulting to 1, 2 and 4 wt.% Pd/SiO_2@Zr catalysts that were evaluated for their diesel oxidation activity and hydrothermal stability.

2. Experimental procedure

Reagents and materials, and characterizations are listed in the Supplementary material.

2.1. Catalysts preparation

The SiO_2@Zr core@shell support was synthesized, with some modifications, as reported previously [3]. The synthesis schematic is shown in Fig. 1. Briefly, monodisperse silica spheres were prepared following the Stöber process [29]. The SiO_2 spheres formed were dispersed in 100 g of ethanol and kept at 30 °C. Afterwards, 0.5 mL of Brij30 solution was added to the SiO_2 suspension and kept stirring for 1 h. Then, 1.8 mL $Zr(BuO)_4$ was added and the solution was stirred overnight at 30 °C. The liquid phase of the colloid was then exchanged for 100 mL DI water (4 times) and aged at room temperature for 3 days. Finally, the SiO_2@Zr spheres were collected after centrifugation followed by drying at 110 °C overnight and calcination at 500 °C for 2 h (10 °C/min).

The resulting SiO_2@Zr support was impregnated with 2.8, 5.6, 11.4 mL $Pd(NH_3)_4(NO_3)_2$ solution (0.0344 M) by wet-impregnation where the pH of the slurry was adjusted to 4 with 0.1 M HNO_3, leading to Pd loadings of 1, 2, and 4 wt.%. The liquid phase of the slurry was then evaporated at room temperature. After the impregnation, the catalyst was dried at 110 °C in air and calcined at 500 °C for 2 h.

2.2 Catalyst evaluation

The performance of the as-synthesized catalysts was evaluated in a customized fixed-bed U-shaped quartz reactor (I.D. = 8 mm) as reported previously [30]. The reactor was placed in a cylindrical furnace surrounded by quartz wool to eliminate heat gradients. A K-type thermocouple was attached outside the reactor, close to the top of the catalyst bed, to allow the PID temperature controller control the furnace temperature. Catalyst powders were pressed and sieved and a final pellet size range between 250 to 500 μm was used to avoid pressure effects during the reaction.

100 mg of catalyst was loaded in the reactor stabilized by two loosely packed quartz wool plugs. Another K-type thermocouple was inserted through the reactor U-tube to the upper quartz wool plug for measuring the inlet gas temperature.

The catalysts were first degreened (DG) (700 °C/4 h) under feed gas composition of 10% O_2, 5% H_2O, 5% CO_2/Ar. Before evaluation, the catalysts were pretreated at 600 °C with 12% O_2, 6% H_2O, 6% CO_2/Ar for 20 min. Diesel oxidation evaluation experiments were performed using the low temperature combustion of diesel (LTC-D) gas composition defined by U.S. DRIVE (Table S1) [8]. The total flow rate was 333 sccm that corresponds to a gas hourly space velocity (GHSV) of 113,000 h^{-1}. CO_2, O_2, H_2, CO, NO, C_2H_4, C_3H_6, C_3H_8 and Ar (UHP, Airgas) were regulated by a set of MKS mass flow controllers. Water was supplied by a D-series pump (Teledyne Isco), evaporated to steam in a tube furnace (200 °C) and carried by Ar to the reactor. Light-off tests were conducted from 100 to 500 °C at a heating rate of 2 °C /min. The effluent gas concentrations were analyzed by an MKS MultiGas 2030 FTIR gas analyzer with a gas cell at 191 °C. The reactor exhaust was diluted with 667 sccm Ar to reduce the response time of the gas analyzer. To avoid water condensation, all the gas lines were heated to 170 °C. Hydrothermal aging (HTA) treatment (800 °C /10 h) was conducted under feed gas composition of 10% O_2, 5% H_2O, 5% CO_2/Ar. Pretreatment and evaluation of the HTA catalysts were performed under the same conditions as the DG catalysts.

3. Results and Discussion

The high-angle annular dark-field scanning transmission electron microscopy (HAADF-STEM) images and energy dispersive X-ray spectroscopy (EDS) elemental maps of fresh (calcined at 500 °C/2 h) 1, 2 and 4 wt.% Pd/SiO_2@Zr catalysts are shown in Fig. 2. Moreover, a 3D tomography video of 1 wt.% Pd/SiO_2@Zr is shown (Video S1). The 3D tomography suggests the

complete coverage of SiO_2 core by Zr-based shell with Pd dispersed on the surface. A spherical structure was confirmed for all studied catalysts (Fig. 2). The EDS elemental maps of Si in Fig. 2a.2, 2b.2 and 2c.2 reveal the successful synthesis of nano-spherical SiO_2 (diameter of about 150 nm) as a support core. The higher density Zr presented as a shell layer (thickness: ~8.4 nm) (Fig. 2a.3, 2b.3 and 2c.3) indicates the successful deposition of Zr species on the SiO_2 core. Palladium is well-dispersed over 1 wt.% Pd/SiO_2@Zr (Fig. 2a.4). However, as Pd loading increased to 2 (Fig. 2b.4) and 4 wt.% (Fig. 2c.4), larger Pd clusters (~5 and 7 nm, respectively) can be observed, possibly due to Pd sintering.

Fig. S1 shows the X-ray diffraction (XRD) patterns of fresh SiO_2@Zr, fresh and HTA (800 ^oC/10 h, 10% O_2, 5% H_2O, 5% CO_2/Ar) 1 wt.% Pd/SiO_2@Zr. All samples display only one broad peak centered at ~23^o, assigned to SiO_2 [31]. No peaks were detected for ZrO_2 over all analyzed samples, suggesting that the majority of Zr in SiO_2@Zr is not present in a ZrO_2 crystalline phase (monoclinic, tetragonal, cube). Moreover, presence of amorphous ZrO_2 is excluded since the samples analyzed by XRD are either fresh (calcined at 500 ^oC) or HTA (exposed to 800 ^oC/10 h) and amorphous ZrO_2 can readily crystallize at T > 300 ^oC [32]. Furthermore, no metallic Pd or PdO peaks were observed over fresh and HTA 1 wt.% Pd/SiO_2@Zr, which might be due to the low loading and the dispersed nature of Pd (Fig. 2a.4).

The surface properties (Brunauer-Emmett-Teller (BET) surface areas and Barrett-Joyner-Halenda (BJH) pore volumes) of SiO_2 core, SiO_2@Zr, and 1 wt.% Pd/SiO_2@Zr are summarized in Table 1. The surface area of fresh SiO_2 core was as low as 2.3 m^2/g. Fresh SiO_2@Zr and 1 wt.% Pd/SiO_2@Zr had improved surface areas of 226.7 and 207.1 m^2/g, respectively. Considering the low surface area of SiO_2 core, the improved surface areas of SiO_2@Zr and 1 wt.% Pd/SiO_2@Zr can be attributed to the Zr-based shell. Furthermore, the surface area loss after HTA was greater

over 1 wt.% Pd/ZrO_2 (fresh: 93 m^2/g, HTA (16 h): 24 m^2/g) [20] than 1 wt.% Pd/SiO_2@Zr (fresh: 226.7 m^2/g, HTA (16 h): 112 m^2/g). The surface area of 1 wt.% Pd/SiO_2@Zr after 10 h of HTA was 104 m^2/g and it remained the same when the HTA time was extended to 16 h (112 m^2/g). This observation suggests that the surface area of Pd/SiO_2@Zr does not change after HTA for 10 h. Moreover, the surface area of Pd/SiO_2@Zr is 4.5 times greater than the one of Pd/ZrO_2 after 16 h of HTA. The significant surface area loss of 1 wt.% Pd/ZrO_2 when exposed to elevated temperatures was attributed to the grain growth of crystalline ZrO_2 [33]. Therefore, the high surface area of SiO_2@Zr and 1 wt.% Pd/SiO_2@Zr after HTA can be attributed to the non-crystalline nature of the Zr-based shell (see XRD data (Fig. S1)). The N_2 adsorption-desorption isotherms of fresh and HTA 1 wt.% Pd/SiO_2@Zr are shown in Fig. S2. Both samples have a type IV isotherm, characteristic of mesoporous materials [34].

Fig. 3 shows the catalytic evaluation results of degreened (DG) 1 wt.% Pd/SiO_2@Zr. 1 wt.% Pd/SiO_2@Zr can achieve 50 and 90% conversions at 168 and 178 °C for CO and 228 and 372 °C for total HCs (THCs), respectively (Fig. 3a). Moreover, 1 wt.% Pd/SiO_2@Zr can reach 50 and 90% conversions at 245 and 362 °C for C_2H_4 and at 192 and 216 °C for C_3H_6, respectively (Fig. 3b). C_3H_8 was converted at a higher temperature (T_{50}= 376 °C, T_{90}= 428 °C) compared to C_2H_4 and C_3H_6, attributed to its stable C-H bonds [35]. The negative conversion of C_3H_8 observed between 180 and 340 °C (Fig. 3b) can be attributed to the desorption of C_3H_8 from PdO [36]. The inflection in CO conversion at 190 °C (Fig. 3a) can be attributed to competition of CO and HCs for active sites and mass transfer limitations [37]. Moreover, the inflection observed in C_2H_4 conversion (Fig. 3b) can be attributed to the adsorption of intermediates formed during C_2H_4 oxidation on Pd active sites (discussed later). These intermediate species can inhibit C_2H_4 adsorption and its further oxidation. Fig. 3c shows the concentrations of NO, NO_2 and N_2O and

their total concentration (= [NO] + [NO_2] + 2[N_2O]) during the evaluation of DG 1 wt.% Pd/SiO_2@Zr. The total concentration of NO, NO_2, and N_2O indicates that most N-containing species were in the form of NO, NO_2, and N_2O. The small negative peak observed at 165 °C can be attributed to N_2 formation (not detectable by the MKS IR). There are three NO consumption peaks at 165, 206 and 471 °C. NO consumed at 165 and 206 °C was converted to N_2 and N_2O, respectively, suggesting that a HC-SCR reaction took place [38]. The third broad NO consumption peak at temperature ~ 471 °C can be attributed to the catalytic NO oxidation over Pd [39] and homogeneous (gas phase) NO oxidation [30].

A hydrothermal aging treatment (800 °C/10 h) was conducted to verify the durability of 1 wt.% Pd/SiO_2@Zr (Fig. 4). Compared to DG 1 wt.% Pd/SiO_2@Zr, HTA 1 wt.% Pd/SiO_2@Zr showed similar T_{50} (168 °C) and T_{90} (178 °C) for CO, while minor deactivation was observed for HC oxidation. Specifically, the T_{50} (207 °C) and T_{90} (372 °C) for THCs was increased by only 21 and 9 °C, respectively, after hydrothermal aging of 1 wt.% Pd/SiO_2@ZrO_2. The ability of 1 wt.% Pd/SiO_2@Zr to achieve a similar performance under DG and HTA conditions highlights the hydrothermal stability of the catalyst. Similarly, the negative conversion of C_3H_8 observed between 180 and 340 °C (Fig. 4b) can be attributed to the desorption of C_3H_8 from PdO [36]. Formaldehyde (CH_2O) was formed at the same temperature range that the inflection in C_2H_4 conversion was observed (Figs. S3a, 4b). The inflection in C_2H_4 conversion was also observed when CO, NO, C_3H_6 and C_3H_8 were removed from the reactor feed (1667 ppm C_2H_4 (C_1 basis), 6% CO_2, 6% H_2O, 12% O_2, and 400 ppm H_2) (Fig. S3b). This observation indicates that intermediates (e.g. CH_2O, CO) formed during C_2H_4 oxidation can be adsorbed on the Pd active sites. The adsorbed intermediates can inhibit C_2H_4 adsorption and thus its further oxidation. Similar NO conversion pattern was observed over both DG and HTA 1 wt.% Pd/SiO_2@Zr (Fig.

4c). The decrease in the total concertation of NO, NO_2, and N_2O can be attributed to HC-SCR reactions [38], as discussed previously.

The effect of Pd loading was investigated by comparing the catalytic performance of 1, 2, and 4 wt.% Pd/SiO_2@Zr (Fig. 5). The CO T_{50}/T_{90}'s were similar at 168/178, 168/179 and 158/172 °C over DG 1, 2 and 4 wt.% Pd/SiO_2@Zr, respectively (Fig. 5a). However, the THC $T_{50,90}$'s decreased as Pd loading increased. Specifically, the THC T_{50}/T_{90}'s decreased from 228/372 °C to 211/355 °C to 191/316 °C over DG 1, 2 and 4 wt.% Pd/SiO_2@Zr, respectively. After hydrothermal aging the T_{50}/T_{90}'s for CO slightly decreased from 165/178 to 163/176 to 163/172 °C with increasing Pd loading from 1 to 2 to 4 wt.% (Fig. 5b). Similarly, the $T_{50,90}$'s for THCs decreased with increasing Pd loading from 1 to 2 to 4 wt.% as follows: 207/381 °C to 202/343 °C to 190/325 °C, respectively.

Fourier transform infrared (FT-IR) spectra were collected over SiO_2 spheres and SiO_2@Zr supports to investigate the support composition and thus the origin of the Pd/SiO_2@Zr thermal stability (Fig. S4). Two peaks at 1101 and 802 cm^{-1} were detected over both SiO_2 spheres and SiO_2@Zr supports, attributed to Si-O-Si bonds [40]. The decrease observed in the transmittance at 965 cm^{-1} over SiO_2@Zr suggested the formation of Si-O-Zr bonds after Zr coating [41]. Moreover, Schüth et al. reported that the bulk and surface Zr/Si molar ratio of the core@shell support was 0.2 and 1, respectively [42]. Si-O-Zr bond formation can hinder the crystallization of the Zr-based shell [43]. Therefore, the improved hydrothermal stability of Pd/SiO_2@Zr can be attributed to the presence of Si-O-Zr.

NO_x-TPD provided an additional indication of the presence of Si-O-Zr bonds over SiO_2@Zr supports. Law et al. showed that there is a linear relationship between NO_x uptake and the accessible ZrO_2 surface area [44, 45]. Thus, NO_x-TPD was conducted to titrate the accessible

surface area of ZrO_2 in SiO_2@Zr. The amount of desorbed NO_x was calculated to be 0.17 μmol $NO_x/m^2_{SiO_2\ @Zr}$ (Fig. 6), which is much lower than that of bare ZrO_2 (5.8 μmol $NO_x/m^2_{ZrO_2}$) [44, 45]. This result indicates that bare ZrO_2 presence on the SiO_2@Zr surface is minimal. This observation is consistent with the SiO_2@Zr XRD data (Fig. S1) where crystallized ZrO_2 was not detected. Moreover, SiO_2@Zr (Fig. 6) and $ZrSiO_4$ (Fig. S5), that contains Si-O-Zr bonds, showed similar NO_x desorption temperatures and NO_x update (0.43 μmol $NO_x/m^2_{ZrSiO_4}$) indicating that the samples have a similar surface composition [46]. Therefore, the low NO_x uptake over SiO_2@Zr can be attributed to the formation of Si-O-Zr bonds on its surface.

4. Conclusions

In this work, a series of hydrothermal stable Pd-based DOCs on a novel SiO_2@Zr support were synthesized. Degreened 1 wt.% Pd/SiO_2@Zr was able to reach 90% CO and THC conversion at 178 and 372 °C, respectively (feed: 6% CO_2, 12% O_2, 6% H_2O, 400 ppm H_2, 2000 ppm CO, 100 ppm NO, 1667 ppm C_2H_4, 1000 ppm C_3H_6, 333 ppm C_3H_8; HC in C_1 basis and GHSV=113,000 h^{-1}). Only a minor decrease in the THC conversion was observed after hydrothermal aging at 800 °C for 10 h (HTA). As the Pd loading increased from 1 to 2 to 4 wt.%, the T_{90}'s for THCs decreased from 372 to 346 to 316 °C, respectively. A similar trend was observed for Pd/SiO_2@Zr after HTA, where the THC T_{90}'s decreased from 381 to 343 to 325 °C with increasing Pd loading from 1 to 2 to 4 wt.% Pd/SiO_2@Zr. The high surface area of Pd/SiO_2@Zr compared to Pd/ZrO_2 before and after HTA was attributed to the poor crystallinity of SiO_2@Zr support. The poor crystallinity of SiO_2@Zr further contributes to the improved hydrothermal stability of Pd/SiO_2@Zr under conditions of low temperature combustion of diesel (LTC-D). Overall, this study revealed the potential of developing high surface area Pd/SiO_2@Zr

catalysts with improved low temperature diesel oxidation performance and enhanced hydrothermal stability.

References:

[1] J. Lee, J.R. Theis, E.A. Kyriakidou, Vehicle emissions trapping materials: Successes, challenges, and the path forward, Appl. Catal. B 243 (2019) 397-414. https://doi.org/10.1016/j.apcatb.2018.10.069.

[2] A.P. Wong, E.A. Kyriakidou, T.J. Toops, J.R. Regalbuto, The catalytic behavior of precisely synthesized Pt–Pd bimetallic catalysts for use as diesel oxidation catalysts, Catal. Today 267 (2016) 145-156. https://doi.org/10.1016/j.cattod.2016.02.011.

[3] E. Kyriakidou, T.J. Toops, J.-S. Choi, M.J. Lance, J.E. Parks II, Exhaust treatment catalysts with enhanced hydrothermal stability and low-temperature activity, US Patents 10,42,137 B2 (October 1, 2019).

[4] M. Zammit, C.L. DiMaggio, C.H. Kim, C. Lambert, G.G. Muntean, C.H. Peden, J.E. Parks, K. Howden, Future automotive aftertreatment solutions: The 150 C challenge workshop report (US Drive Workshop, 2012) https://www.pnnl.gov/main/publications/external/technical_Reports/PNNL-22815.pdf.

[5] Y. Shin, Y. Jung, C.P. Cho, Y.D. Pyo, J. Jang, G. Kim, T.M. Kim, NO_x abatement and N_2O formation over urea-SCR systems with zeolite supported Fe and Cu catalysts in a nonroad diesel engine, Chem. Eng. J. 381 (2020) 122751. https://doi.org/10.1016/j.cej.2019.122751.

[6] B. Apicella, E. Mancaruso, C. Russo, A. Tregrossi, M.M. Oliano, A. Ciajolo, B.M. Vaglieco, Effect Of After-Treatment Systems On Particulate Matter Emissions In Diesel Engine Exhaust, Exp. Therm. Fluid Sci. (2020) 110107. https://doi.org/10.1016/j.expthermflusci.2020.110107.

[7] A. Ko, Y. Woo, J. Jang, Y. Jung, Y. Pyo, H. Jo, O. Lim, Y.J. Lee, Complementary effects between NO oxidation of DPF and NO_2 decomposition of SCR in light-duty diesel engine, J. Ind. Eng. Chem. 80 (2019) 160-170. https://doi.org/10.1016/j.jiec.2019.07.045.

[8] K.G. Rappé, C. DiMaggio, J.A. Pihl, J.R. Theis, S.H. Oh, G.B. Fisher, J. Parks, V.G. Easterling, M. Yang, M.L. Stewart, Aftertreatment Protocols for Catalyst Characterization and Performance Evaluation: Low-Temperature Oxidation, Storage, Three-Way, and NH_3-SCR Catalyst Test Protocols, Emiss. Control Sci. Technol. 5(2) (2019) 183-214. https://doi.org/10.1007/s40825-019-00120-7.

[9] S. Du, W. Tang, Y. Guo, A. Binder, E.A. Kyriakidou, T.J. Toops, S. Wang, Z. Ren, S. Hoang, P.-X. Gao, Understanding low temperature oxidation activity of nanoarray-based monolithic catalysts: from performance observation to structural and chemical insights, Emiss. Control Sci. Technol. 3(1) (2017) 18-36. https://doi.org/10.1007/s40825-016-0054-y.

[10] S. Hoang, Y. Guo, A.J. Binder, W. Tang, S. Wang, J.J. Liu, T.D. Huan, X. Lu, Y. Wang, Y. Ding, Activating low-temperature diesel oxidation by single-atom Pt on TiO_2 nanowire array, Nat. Commun. 11(1) (2020) 1-10. https://doi.org/10.1038/s41467-020-14816-w.

[11] Y. Xie, E. Rodrigues, N. Furtado, A. Matynia, T. Arlt, P. Rodatz, P. Da Costa, Aging of commercial diesel oxidation catalysts: a preliminary structure/reactivity study, Top. Catal. 59(10-12) (2016) 1039-1043. https://doi.org/10.1007/s11244-016-0586-y.

[12] D. Kunwar, C. Carrillo, H. Xiong, E. Peterson, A. DeLaRiva, A. Ghosh, G. Qi, M. Yang, M. Wiebenga, S. Oh, Investigating Anomalous Growth of Platinum Particles during Accelerated Aging of Diesel Oxidation Catalysts, Appl. Catal. B 266 (2020) 118598. https://doi.org/10.1016/j.apcatb.2020.118598.

[13] C. Carrillo, A. DeLaRiva, H. Xiong, E.J. Peterson, M.N. Spilde, D. Kunwar, R.S. Goeke, M. Wiebenga, S.H. Oh, G. Qi, S.R. Challa, A.K. Datye, Regenerative trapping: How Pd improves the durability of Pt diesel oxidation catalysts, Appl. Catal. B 218 (2017) 581-590. https://doi.org/10.1016/j.apcatb.2017.06.085.

[14] J. Liu, B. Qiao, Y. Song, Y. Huang, J.J. Liu, Hetero-epitaxially anchoring Au nanoparticles onto ZnO nanowires for CO oxidation, Chem. Comm. 51(83) (2015) 15332-15335. https://doi.org/10.1039/C5CC03353E.

[15] Y. Sun, W. Liu, M. Tian, L. Wang, Z. Wang, A Rational Design of the Sintering-Resistant Au-CeO_2 Nanoparticles Catalysts for CO Oxidation: The Influence of H_2 Pretreatments, Materials 11(10) (2018) 1952. https://doi.org/10.3390/ma11101952.

[16] G.J. Kim, D.W. Kwon, S.C. Hong, Effect of Pt particle size and valence state on the performance of Pt/TiO_2 catalysts for CO oxidation at room temperature, J. Phys. Chem. C 120(32) (2016) 17996-18004. https://doi.org/10.1021/acs.jpcc.6b02945.

[17] Q. Guo, R. Joyner, An X-ray photoelectron spectroscopy study of the stability of ZrO_2 films on Pd (110), Appl. Surf. Sci. 144 (1999) 375-379. https://doi.org/10.1016/S0169-4332(98)00827-7.

[18] J. Bitter, K. Seshan, J. Lercher, On the contribution of X-ray absorption spectroscopy to explore structure and activity relations of Pt/ZrO_2 catalysts for CO_2/CH_4 reforming, Top. Catal. 10(3-4) (2000) 295-305. https://doi.org/10.1023/A:1019149025242.

[19] C. Dall'Agnol, A. Gervasini, F. Morazzoni, F. Pinna, G. Strukul, L. Zanderighi, Hydrogenation of carbon monoxide: Evidence of a strong metal-support interaction in RhZrO_2 catalysts, J. Catal. 96(1) (1985) 106-114. https://doi.org/10.1016/0021-9517(85)90364-1.

[20] M.-Y. Kim, E.A. Kyriakidou, J.-S. Choi, T.J. Toops, A.J. Binder, C. Thomas, J.E. Parks II, V. Schwartz, J. Chen, D.K. Hensley, Enhancing low-temperature activity and durability of Pd-based diesel oxidation catalysts using ZrO_2 supports, Appl. Catal. B 187 (2016) 181-194. https://doi.org/10.1016/j.apcatb.2016.01.023.

[21] D. Aguilar, L. Torres-Gonzalez, L. Torres-Martinez, T. Lopez, P. Quintana, A study of the crystallization of ZrO_2 in the sol–gel system: ZrO_2–SiO_2, J. Solid State Chem. 158(2) (2001) 349-357. https://doi.org/10.1006/jssc.2001.9126.

[22] G. Dingemans, A. Clark, J. Van Delft, M. Van De Sanden, W. Kessels, Er^{3+} and Si luminescence of atomic layer deposited Er-doped Al_2O_3 thin films on Si (100), J. Appl. Phys. 109(11) (2011) 113107. https://doi.org/10.1063/1.3595691.

[23] V. Nagarajan, K. Rao, Crystallization studies of ZrO_2–SiO_2 composite gels, J. Mater. Sci. 24(6) (1989) 2140-2146. https://doi.org/10.1007/BF02385434.

[24] T. Ono, M. Kagawa, Y. Syono, Ultrafine particles of the ZrO_2-SiO_2 system prepared by the spray-ICP technique, J. Mater. Sci. 20(7) (1985) 2483-2487. https://doi.org/10.1007/BF00556078.

[25] C. Zhao, O. Richard, H. Bender, M. Caymax, S. De Gendt, M. Heyns, E. Young, G. Roebben, O. Van der Biest, S. Haukka, Miscibility of amorphous ZrO_2–Al_2O_3 binary alloy, Appl. Phys. Lett. 80(13) (2002) 2374-2376. https://doi.org/10.1063/1.1459765.

[26] G. Balakrishnan, A. Wasy, H.S. Ho, P. Sudhakara, S. Bae, J. Song, Study of Al_2O_3/ZrO_2 (5 nm/20nm) Nanolaminate Composite, Compos. Res. 26(1) (2013) 60-65. https://doi.org/10.7234/kscm.2013.26.1.60.

[27] M.-Y. Kim, J.-S. Choi, T.J. Toops, E.-S. Jeong, S.-W. Han, V. Schwartz, J. Chen, Coating SiO_2 support with TiO_2 or ZrO_2 and effects on structure and CO oxidation performance of Pt catalysts, Catalysts 3(1) (2013) 88-103. https://doi.org/10.3390/catal3010088.

[28] D.P. Nolan, Fire Pump Arrangements at Industrial Facilities, third ed., Gulf Professional Publishing, Oxford, 2017.

[29] W. Stöber, A. Fink, E. Bohn, Controlled growth of monodisperse silica spheres in the micron size range, J. Colloid Interface Sci. 26(1) (1968) 62-69. https://doi.org/10.1016/0021-9797(68)90272-5.

[30] C.-H. Liu, K. Giewont, T.J. Toops, E.A. Walker, C. Horvatits, E.A. Kyriakidou, Non-catalytic gas phase NO oxidation in the presence of decane, Fuel 286 (2021) 119388. https://doi.org/10.1016/j.fuel.2020.119388.

[31] S. Musić, N. Filipović-Vinceković, L. Sekovanić, Precipitation of amorphous SiO_2 particles and their properties, Braz. J. Chem. Eng. 28(1) (2011) 89-94. https://doi.org/10.1590/S0104-66322011000100011.

[32] S. Tada, S. Kayamori, T. Honma, H. Kamei, A. Nariyuki, K. Kon, T. Toyao, K.-i. Shimizu, S. Satokawa, Design of interfacial sites between Cu and amorphous ZrO_2 dedicated to CO_2-to-methanol hydrogenation, ACS Catalysis 8(9) (2018) 7809-7819. https://pubs.acs.org/doi/abs/10.1021/acscatal.8b01396.

[33] F. Lu, J. Zhang, M. Huang, F. Namavar, R.C. Ewing, J. Lian, Phase transformation of nanosized ZrO2 upon thermal annealing and intense radiation, J. Phys. Chem. C 115(15) (2011) 7193-7201. https://doi.org/10.1021/jp109558s.

[34] K.S. Sing, Reporting physisorption data for gas/solid systems with special reference to the determination of surface area and porosity (Recommendations 1984), Pure Appl. Chem. 57(4) (1985) 603-619.

[35] R.G. Bergman, C–H activation, Nature 446(7134) (2007) 391-393. https://doi.org/10.1038/446391a.

[36] S.S. Kum, B.Y. Jo, S.H. Moon, Performance of Pd-promoted Mo–V–Te–Nb–O catalysts in the partial oxidation of propane to acrylic acid, Appl. Catal., A 365(1) (2009) 79-87. https://doi.org/10.1016/j.apcata.2009.05.056.

[37] P. Piqueras, A. García, J. Monsalve-Serrano, M.J. Ruiz, Performance of a diesel oxidation catalyst under diesel-gasoline reactivity controlled compression ignition combustion conditions, Energy Convers. Manag. 196 (2019) 18-31. https://doi.org/10.1016/j.enconman.2019.05.111.

[38] R. Burch, J. Breen, F. Meunier, A review of the selective reduction of NOx with hydrocarbons under lean-burn conditions with non-zeolitic oxide and platinum group metal catalysts, Appl. Catal. B 39(4) (2002) 283-303. https://doi.org/10.1016/S0926-3373(02)00118-2.

[39] X. Auvray, L. Olsson, Stability and activity of Pd-, Pt-and Pd–Pt catalysts supported on alumina for NO oxidation, Appl. Catal. B 168 (2015) 342-352. https://doi.org/10.1016/j.apcatb.2014.12.035.

[40] T. Zhang, J. Ge, Y. Hu, Q. Zhang, S. Aloni, Y. Yin, Formation of hollow silica colloids through a spontaneous dissolution–regrowth process, Angew. Chem. 120(31) (2008) 5890-5895. https://doi.org/10.1002/ange.200800927.

[41] N. Hassan, A. Jalil, N. Khusnun, M. Ali, S. Haron, Role of reduced graphene oxide in improving interfacial charge transfer of hybridized rGO/silica/zirconia for enhanced Bisphenol A photodegradation, J. Alloys Compd. 789 (2019) 221-230. https://doi.org/10.1016/j.jallcom.2019.03.105.

[42] P.M. Arnal, C. Weidenthaler, F. Schüth, Highly monodisperse zirconia-coated silica spheres and zirconia/silica hollow spheres with remarkable textural properties, Chem. Mater. 18(11) (2006) 2733-2739. https://doi.org/10.1021/cm052580a.

[43] S. Kongwudthiti, P. Praserthdam, W. Tanakulrungsank, M. Inoue, The influence of Si–O–Zr bonds on the crystal-growth inhibition of zirconia prepared by the glycothermal method, J. Mater. Process. Technol. 136(1-3) (2003) 186-189. https://doi.org/10.1016/S0924-0136(03)00157-2.

[44] H.Y. Law, J. Blanchard, X. Carrier, C. Thomas, NO_x-TPD as a Tool to Estimate the Accessible Zirconia Surface of ZrO_2-Containing Materials, J. Phys. Chem. C 114(21) (2010) 9731-9738. https://doi.org/10.1021/jp9089535.

[45] C. Thomas, Should W Surface Density of WO_x–ZrO_2 Catalysts Be Calculated With Respect To the Specific Surface Area of the Sample or That of ZrO_2 Only?, J. Phys. Chem. C 115(5) (2011) 2253-2256. https://doi.org/10.1021/jp110497e.

[46] M. Ogura, R. Guillet-Nicolas, D. Brouri, S. Casale, J. Blanchard, K.A. Cychosz, M. Thommes, C. Thomas, Insights into the accessibility of Zr in Zr/SBA-15 mesoporous silica supports with increasing Zr loadings, Micropor. Mesopor. Mat. 225 (2016) 440-449. https://doi.org/10.1016/j.micromeso.2016.01.026.

Table 1. BET surface areas and BJH pore volumes of SiO_2 core, SiO_2@Zr, and (fresh, HTA) 1 wt.% Pd/SiO_2@Zr.

	BET surface area (m^2/g)	BJH pore volume (cm^3/g)
Fresh SiO_2	2.3	0.009
Fresh SiO_2@Zr	226.7	0.170
Fresh 1 wt.% Pd/SiO_2@Zr	207.2	0.152
HTA 1 wt.% Pd/SiO_2@Zr	103.9	0.089

Fig. 1. Synthesis of SiO_2@Zr core@shell support using a hard template method.

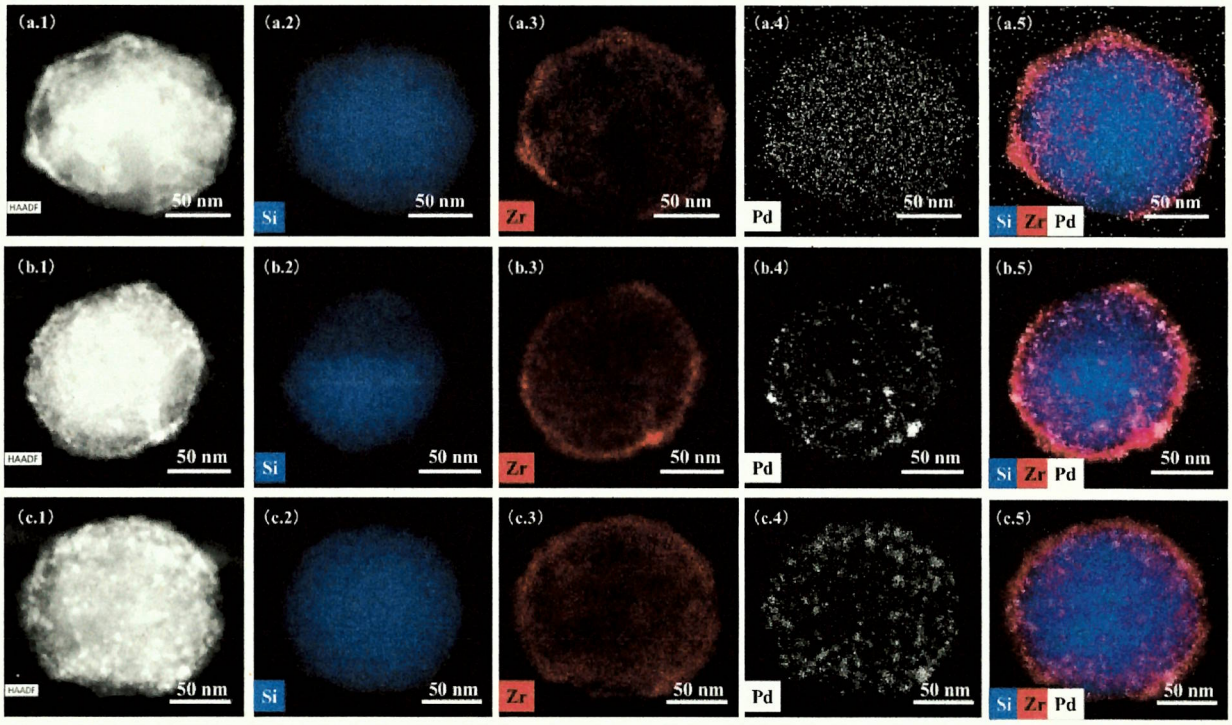

Fig. 2. HAADF-STEM images and EDS elemental maps of fresh (a.1-5) 1 wt.% Pd/SiO_2@Zr, (b.1-5) 2 wt.% Pd/SiO_2@Zr, and (c.1-5) 4 wt.% Pd/SiO_2@Zr catalysts.

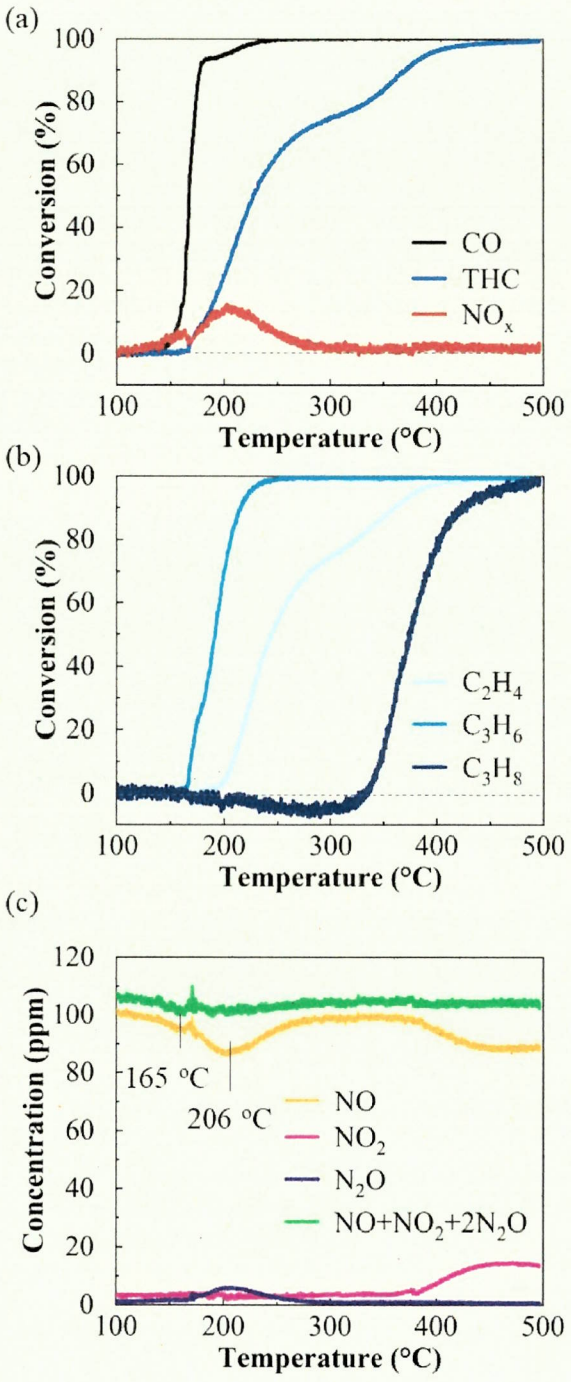

Fig. 3. (a) CO, THC, NO_x, (b) C_2H_4, C_3H_6, C_3H_8 conversions and (c) NO, NO_2, N_2O concentrations and their total concentration (= [NO] + [NO_2] + 2[N_2O]) as a function of temperature of degreened 1 wt.% Pd/SiO_2@Zr.

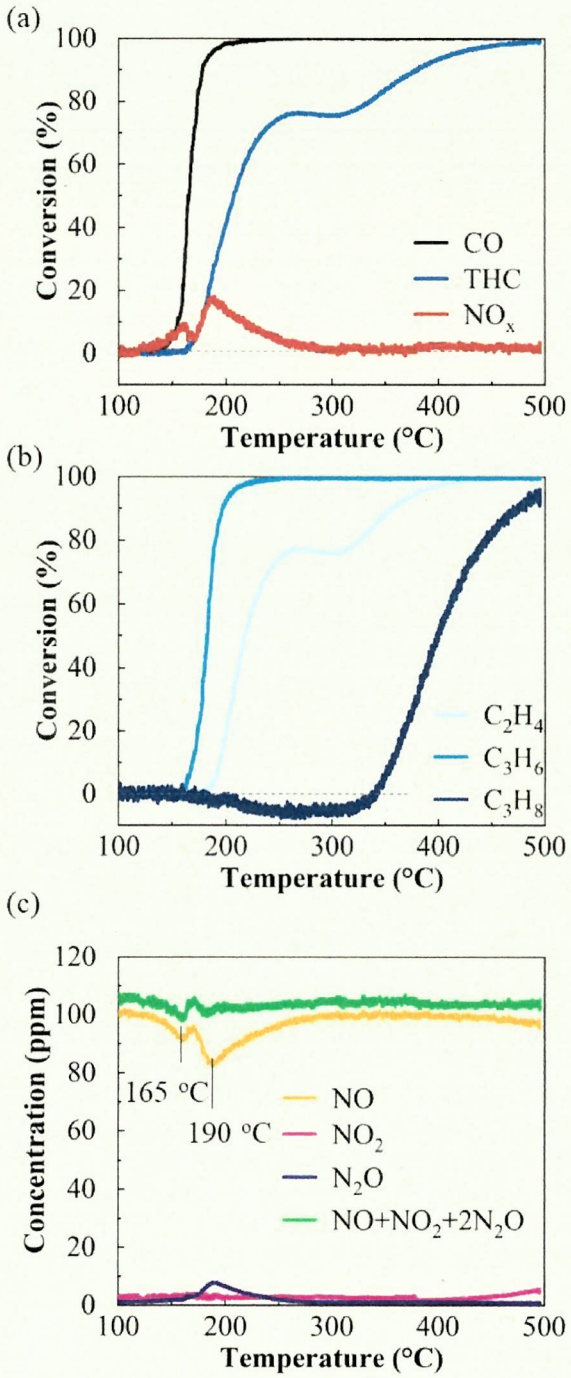

Fig. 4. (a) CO, THC, NO_x, (b) C_2H_4, C_3H_6, C_3H_8 conversions and (c) NO, NO_2, N_2O concentrations and their total concentration (= [NO] + [NO_2] + 2[N_2O]) as a function of temperature of hydrothermally aged 1 wt.% Pd/SiO_2@Zr.

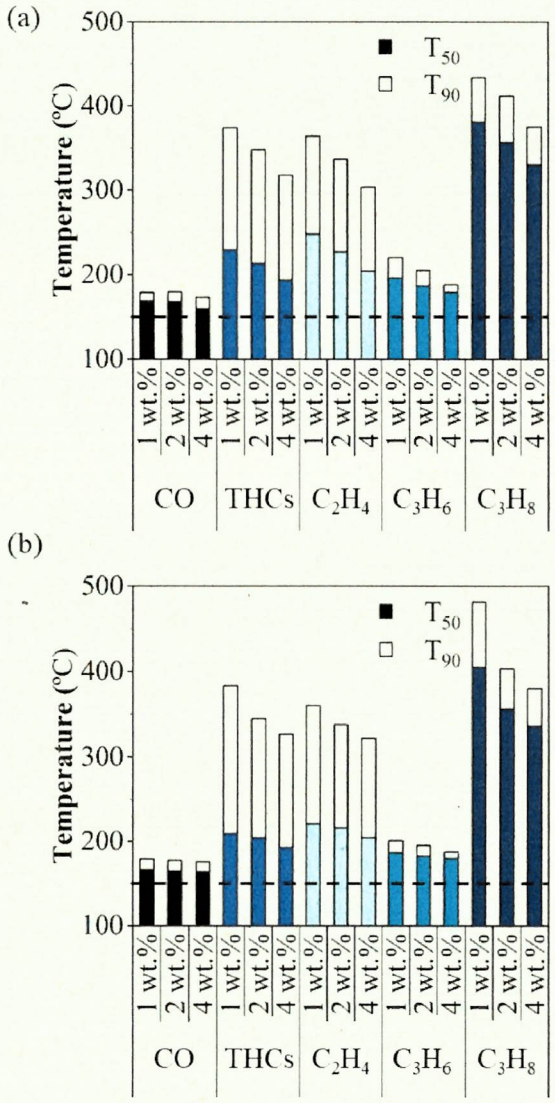

Fig. 5. Comparison of $T_{50,90}$'s of CO, THCs, C_2H_4, C_3H_6, C_3H_8 over (a) degreened and (b) hydrothermally aged 1, 2, 4 wt.% Pd/SiO_2@Zr catalysts. The horizontal dashed line denotes the 150 °C target temperature for achieving 90% conversion.

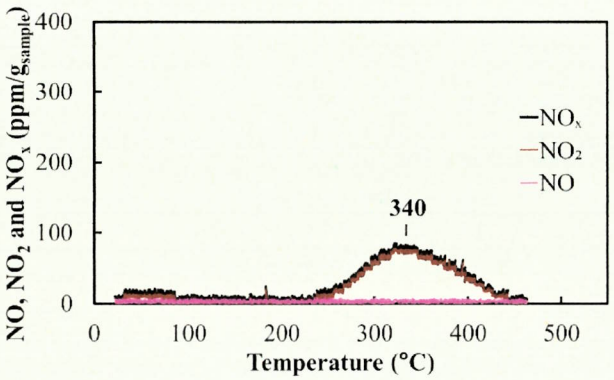

Fig. 6. NO_x-TPD profiles over fresh SiO_2@Zr.

Supplementary material

Hydrothermally Stable Pd/SiO_2@Zr Core@Shell Catalysts for Diesel Oxidation Applications

ChihHan Liu[a,+], Junjie Chen[a,+], Todd J. Toops[b], Jae-Soon Choi[b,1], Cyril Thomas[c], Michael J. Lance[b], and Eleni A. Kyriakidou[a,*]

[a] *Department of Chemical and Biological Engineering, University at Buffalo, The State University of New York, Buffalo, NY 14260, USA*

[b] *Oak Ridge National Laboratory, Oak Ridge, TN 37831, USA*

[c] *Sorbonne Université, CNRS, Laboratoire de Réactivité de Surface (LRS), 4 Place Jussieu, F-75252 Paris, France*

[+]These authors contributed equally to this work

[1]Present address: Catalyst Development Center, Basic Materials and Chemicals R&D, LG Chem, Daejeon, Korea.

[*]Corresponding author at: elenikyr@buffalo.edu (E.A. Kyriakidou)

Table of Contents

Reagents and materials

Zirconium(IV) butoxide solution ($Zr(BuO)_4$) (80 wt.% in 1-butanol, Sigma-Aldrich), tetraethyl orthosilicate (TEOS) (98% purity, Strem), anhydrous ethyl alcohol (200 proof, Decon), ammonium hydroxide (NH_4OH, 28-30 wt.% solution of NH_3 in water, Sigma-Aldrich), nitric acid (65 wt.%, Fisher) and tetraamminepalladium nitrate ($Pd(NH_3)_4(NO_3)_2$) (10% in H_2O, Sigma-Aldrich), zirconium silicate (98%, ACROS) were used as received. Brij30 (ACROS) was diluted with DI water to a 3.76 wt.% Brij30 solution prior to usage. Nitric acid was diluted with DI water to 0.1 M prior to usage. DI water purified to 18.2 MΩ•cm (Milli-Q grade) was used for all reported synthesis.

Characterizations

HAADF-STEM images and EDS elemental maps of $Pd/SiO_2@Zr$ catalysts were obtained with a FEI Talos F200X STEM. The catalysts were first dispersed in isopropyl alcohol under ultrasonication for 15 minutes. One drop of the solution was added onto carbon-coated copper TEM grids followed by drying in air at ambient temperature.

The BET surface areas and BJH pore volumes of the studied samples were determined by N_2 physisorption with a Micromeritics Tri-Star II surface area and porosity analyzer. Before the measurement, all the samples were degassed at 150 °C for 2 h.

XRD was conducted in a Rigaku Ultima IV using a Cu-Kα X-ray source (wavelength: 0.15406 nm) operating at 40 kV, 44 mA. XRD patterns were collected in a 2θ range of 5-85°, with a scan rate of 2°/min.

Fourier transform infrared (FT-IR) spectra of SiO_2 spheres and $SiO_2@Zr$ were collected between 400-4000 cm^{-1} with a Bruker Vertex 70 FTIR spectrophotometer.

NO_x-TPD experiments were conducted following the procedure reported previously [1]. The catalysts (~500 mg) were first loaded in a U-shaped quartz reactor (I.D. = 15 mm) and pretreated at 500 °C /2 h with 100 sccm (100 mL/min, STP) 20% O_2/He. After cooling down to room temperature, the samples were exposed to the adsorption mixture (400 ppm NO_x and 8% O_2/He) for ~ 200 min. The samples were then purged with 8% O_2/He (230 sccm) to remove gas phase NO_x until negligible NO and NO_2 were detected at the reactor outlet, followed by heating up to 560 °C (3 °C /min) to perform the NO_x-TPD experiments. The NO and NO_2 concentrations were recorded by a chemiluminescence NO_x analyzer (42C-HT, Thermo Environmental Instruments). A correction for the weight loss due to dehydration of the samples was conducted for the NO_x-TPD profiles.

Table S1. Simulated exhaust for low temperature combustion of diesel (LTC-D) based on the low temperature oxidation protocol by U.S. Drive [2], balance Ar.

Components	**Concentration**
O_2	12%
H_2O	6%
CO_2	6%
H_2	400 ppm
CO	2000 ppm
NO	100 ppm
Hydrocarbon - on C_1 basis	
Total HCs	3000 ppm
C_2H_4	1667 ppm
C_3H_6	1000 ppm
C_3H_8	333 ppm

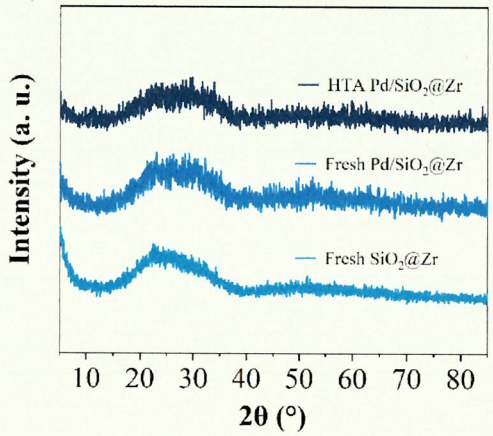

Fig. S1. XRD patterns of fresh SiO_2@Zr, fresh and HTA 1 wt.% Pd/SiO_2@Zr.

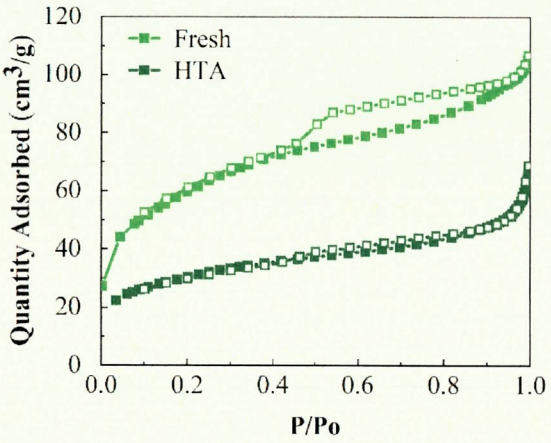

Fig. S2. N_2 adsorption (solid) – desorption (open) isotherms of fresh and HTA 1 wt.% Pd/SiO_2@Zr.

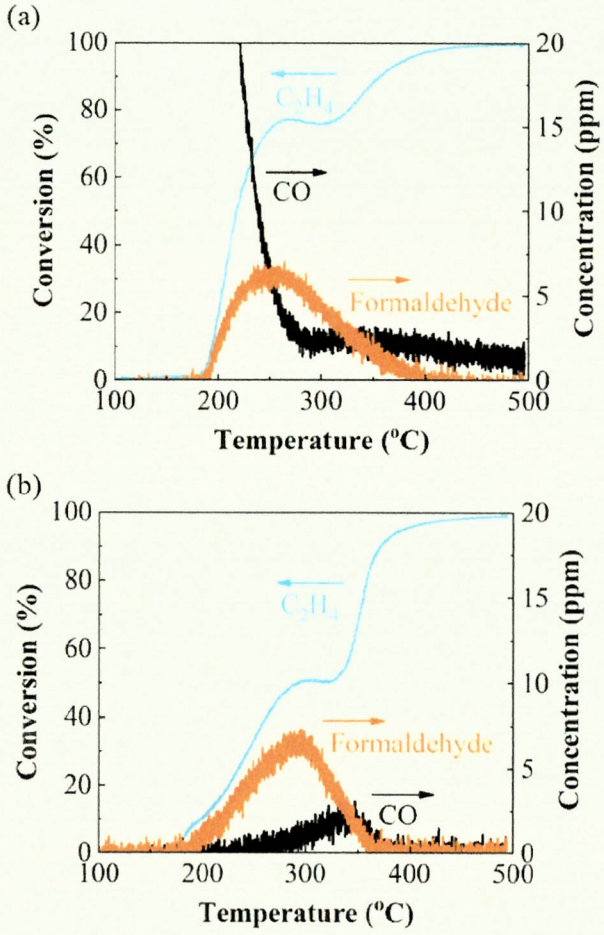

Fig. S3. C_2H_4 conversion (left y-axis) and CO, formaldehyde concentrations (right y-axis) over hydrothermally aged 1 wt.% Pd/SiO_2@Zr under reactor feed containing (a) 6% CO_2, 12% O_2, 6% H_2O, 400 ppm H_2, 2000 ppm CO, 100 ppm NO, 1667 ppm C_2H_4, 1000 ppm C_3H_6, 333 ppm C_3H_8 and (b) 6% CO_2, 12% O_2, 6% H_2O, 400 ppm H_2, 1667 ppm C_2H_4; HCs in C_1 basis. The slow light-off profile of C_2H_4 in Fig. S3b compared to Fig. S3a can be attributed to the decreased exothermic effect when C_3H_6, C_3H_8, and CO were removed from the reactor feed (data not shown).

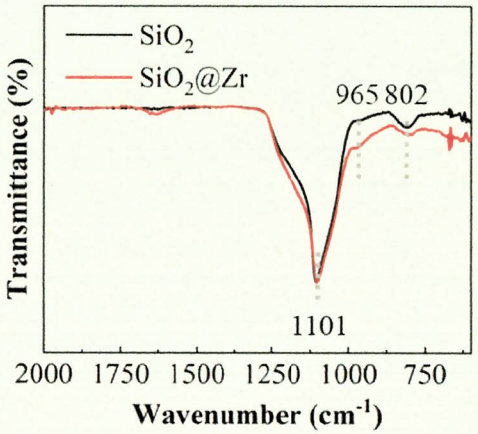

Fig. S4. FT-IR spectra of SiO_2 spheres and SiO_2@Zr support.

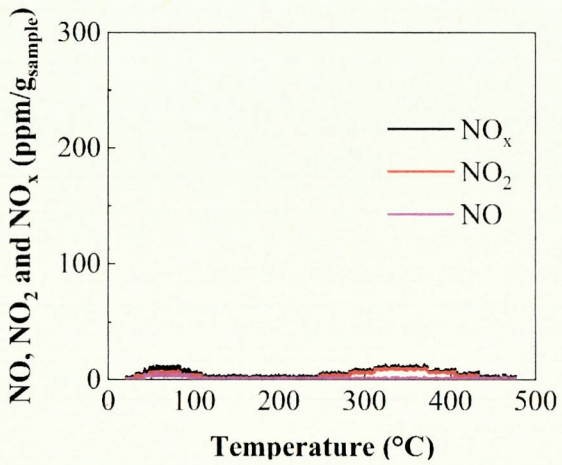

Fig. S5. NO_x-TPD profiles over fresh $ZrSiO_4$.

Video. S1. 3D tomography video of 1 wt.% Pd/SiO_2@Zr.

References:

[1] H.Y. Law, J. Blanchard, X. Carrier, C. Thomas, NO_x-TPD as a Tool to Estimate the Accessible Zirconia Surface of ZrO_2-Containing Materials, J. Phys. Chem. C 114(21) (2010) 9731-9738. https://doi.org/https://doi.org/10.1021/jp9089535.

[2] K.G. Rappé, C. DiMaggio, J.A. Pihl, J.R. Theis, S.H. Oh, G.B. Fisher, J. Parks, V.G. Easterling, M. Yang, M.L. Stewart, Aftertreatment Protocols for Catalyst Characterization and Performance Evaluation: Low-Temperature Oxidation, Storage, Three-Way, and NH_3-SCR Catalyst Test Protocols, Emiss. Control Sci. Technol. 5(2) (2019) 183-214. https://doi.org/https://doi.org/10.1007/s40825-019-00120-7.